



Interface self-referenced dynamic full-field optical coherence tomography

TUAL MONFORT,^{1,2} SALVATORE AZZOLLINI,¹  TASNIM BEN YACOUB,¹ ISABELLE AUDO,¹ SACHA REICHMAN,¹ KATE GRIEVE,^{1,2,†} AND OLIVIER THOUVENIN^{3,†*} 

¹Sorbonne Université, INSERM, CNRS, Institut de la Vision, 17 rue Moreau, F-75012 Paris, France

²CHNO des Quinze-Vingts, INSERM-DGOS CIC 1423, 28 rue de Charenton, F-75012 Paris, France

³Institut Langevin, ESPCI Paris, Université PSL, CNRS, 75005 Paris, France

[†]These authors contributed equally

*olivier.thouvenin@espci.fr

Abstract: Dynamic full-field optical coherence tomography (D-FFOCT) has recently emerged as an invaluable live label-free and non-invasive imaging modality able to image subcellular biological structures and their metabolic activity within complex 3D samples. However, D-FFOCT suffers from fringe artefacts when imaging near reflective surfaces and is highly sensitive to vibrations. Here, we present interface Self-Referenced (iSR) D-FFOCT, an alternative configuration to D-FFOCT that takes advantage of the presence of the sample coverslip in between the sample and the objective by using it as a defocused reference arm, thus avoiding the aforementioned artefacts. We demonstrate the ability of iSR D-FFOCT to image 2D fibroblast cell cultures, which are among the flattest mammalian cells.

© 2023 Optica Publishing Group under the terms of the [Optica Open Access Publishing Agreement](#)

1. Introduction

In recent years, optical coherence tomography (OCT) has emerged as a versatile non-invasive label free optical imaging technique thanks to its high resolution, amplitude and phase contrasts [1–4], its sectioning ability, its sensitivity and imaging speed [2–5]. OCT takes advantage of low coherence interferometric detection of the light backscattered by sample structures to amplify and detect extremely small signals—down to 10^{12} of the incident power [6,7]—to achieve optical sectioning [1] and quantitative phase imaging [8,9]. In time domain OCT (TD OCT) [10], the entire spectrum is integrated on the detector so that optical interference is only localized around the zero optical path difference. Detecting only the interference enables the axial localization of scattering structures, i.e. optical sectioning, independently from the axial diffraction limit. In Fourier domain OCT (FD OCT) [11], the interference spectrogram is measured, and the scattering potential along an axial column inside the sample can be measured by an inverse Fourier transform [11]. FD OCT techniques include both spectral domain OCT (SD OCT) [11], where the interference spectrogram is captured by a spectrometer in a single acquisition, and swept source OCT (SS OCT) [12] where a tunable wavelength light source sweeps its central wavelength, and interference patterns at different wavelengths are successively acquired [12]. In a general manner, FD OCT often has higher sensitivity and higher acquisition speed than conventional point scanning TD OCT thanks to the parallel detection of all depths of the sample [7,13]. Advantageously, FD OCT rapidly acquires axial scans, which enables one to measure and compensate for sample-induced axial movements, which is a critical aspect for retinal imaging for example [14]. However, in order to efficiently image the entire axial depth offered by the spectral resolution, the depth of field has to be large enough, and thus most FD OCT systems are operated at low numerical aperture (NA), implying low transverse resolution.

In contrast, TD OCT images point-by-point with an overlapping focal plane and coherence volume. This is naturally more adapted to the use of high NA objectives, and transverse and

axial resolutions below one micron have been reported on a faster version of TD OCT called TD full-field OCT [4,5,15,16]—referred to as full-field OCT (FFOCT) on the rest of the manuscript. FFOCT images one transverse plane in a single shot [17] rather than scanning point-by-point. However, a spatially incoherent light source needs to be used to avoid crosstalks [18] and compensate the absence of a spatial pinhole. FFOCT has been demonstrated *in vivo* on living rodent for single myelin resolution sheath disruption involved in neuropathies [19], as well as *in vivo* on human retina [20] and cornea [21] with cellular-resolution capabilities.

One promising recent development of FFOCT is dynamic FFOCT (D-FFOCT), in which the temporal evolution of FFOCT signal is analysed in order to quantify the nanometric active displacements of subcellular organelles [15,16,22–25]. D-FFOCT provides a metabolic contrast [2,23,24] highly complementary to the structural contrast obtained from static FFOCT [25]. Static and dynamic FFOCT ((D)-FFOCT) have been combined for several *in vitro* and *ex vivo* studies, for example in retinal explants [16,24,26] and retinal organoids [16,23]. Taking advantage of morphology and specific dynamic contrast, (D)-FFOCT could resolve different cell types and metabolic states. Although similar contrast has been recently demonstrated with dynamic FD-OCT [27], the high spatial resolution accessible with (D)-FFOCT enables one to resolve subcellular structures [2,16,23,24,28,29], including nucleus shape and activity which enables the monitoring of senescent and mitotic cells [16,24,29]. As a result, (D)-FFOCT is an appealing solution to drive biology research on unaltered systems at high resolution under live imaging conditions [16,23,29].

Despite its success, a few aspects still impede (D)-FFOCT. Based on a Linnik interferometer configuration, (D)-FFOCT relies on two symmetric but physically separated optical arms. This aspect leads to three main drawbacks; first, (D)-FFOCT is prone to fringe artefacts when imaging close to the reflective surface of sample holders for *ex vivo* and *in vitro* studies [24,28–31] typically preventing imaging of the first micrometers of a sample, which especially impacts the imaging of thin samples. Yet, adherent (2D) cell culture is the main *in vitro* condition used in biology [32–34]. Groux *et al.* were recently able to partially suppress these fringe artefacts by using weakly scattering porous polycarbonate transwell membranes to move the sample away from the sample holder in 2D retina pigmented epithelial (RPE) cell cultures [29]. Nonetheless, for thinner epithelial cells (<5 μm thick), such as fibroblasts, the signal from the transwell membranes partially covers the cell bodies and decreases image quality. Also, these transwell membranes are incompatible with the highest numerical aperture (NA) objectives due to their limited working distance, and are not adapted to all cell culture conditions and protocols. Second, D-FFOCT is sensitive to subnanometric external vibrations which, even on specifically designed vibration-free optical tables, are hard to cancel completely. This reduces the image quality of D-FFOCT and makes it difficult to properly quantify the organelle motion and the metabolic contrast [24]. Finally, (D)-FFOCT is challenging to implement using objectives with very high numerical aperture (>1), or when the interference arms contain several optical elements [16]. Indeed, any dissymmetry, including spherical aberration due to small misalignments between interfering fields results in distortions, a loss of accessible field of view, and a loss of interference contrast [16]. This typically results in non-homogeneous and distorted (D)-FFOCT signal over the field of view, which makes efficient mosaicking complicated to implement [16].

In this work we present and characterize an alternative interferometric configuration which overcomes these (D)-FFOCT drawbacks in order to enable imaging of cells in the vicinity of the culture surface. Instead of using an external reference arm, *interface Self-Referenced* (iSR) (D)-FFOCT uses the glass coverslip on which the cell culture is performed as the reference mirror. Although a similar strategy was already reported in FD OCT [8,9], previous work had used a relatively low NA and axial resolution of a few micrometers imposing the use of the coverslip surface further from the sample, referred to as the coverslip top surface. The relatively low axial resolution prevented direct amplitude imaging of cell details in flat samples attached to

the bottom coverslip surface, and only quantitative phase imaging of the light passing through the entire cell was accessible in this configuration. Here, to our knowledge, we present the first demonstration of the use of the glass coverslip as the reference arm in TD OCT, and in particular in FFOCT, as well as for dynamic OCT applications. The high axial resolution of less than 1 μm allows imaging of scattering structures in the vicinity of the bottom coverslip surface. We demonstrate that this configuration is also compatible with and highly advantageous for dynamic OCT. iSR (D)-FFOCT allowed imaging of flat 2D fibroblast samples, which are of interest to biologists in disease modelling applications of mitochondrial disease [35–38]. The technique could be used more widely for rapid and robust diagnosis directly from cell phenotypes, with the same contrast as in (D)-FFOCT.

2. Methods

2.1. FFOCT and iSR FFOCT microscopes

FFOCT measurements were performed using the setup described in [16], and shown in a simplified form in Fig. 1. A high-power LED S_1 (either a M810L3 or M730L4, Thorlabs, Newport, NJ, USA, $\lambda_0 = 810 \text{ nm}$ $\Delta\lambda = 25 \text{ nm}$, coherence length $L_c = 8.7 \mu\text{m}$ or $\lambda_0 = 730 \text{ nm}$ $\Delta\lambda = 40 \text{ nm}$, coherence length $L_c = 4.4 \mu\text{m}$), was used to illuminate a Linnik interferometer with high NA objectives (NA = 1.05, immersion medium $n = 1.4$, silicon oil, UPLSAPO30XSIR, Olympus, Japan). The light reflected by the reference mirror, the light reflected by the glass coverslip supporting the sample, and the light backscattered by the sample are recombined by the non-polarizing beamsplitter, focused by a tube lens L3 (AC254-300-B-ML, Thorlabs, Newport, NJ, USA) to overlap, and potentially interfere, on a high full well capacity (FWC) 2D CMOS sensor (Q-2HFW, Adimec, Netherland). The lateral and axial magnifications of the system are respectively: $\gamma_t = 58$, $\gamma_L = 2400$.

iSR FFOCT measurements were performed on the same setup by manually blocking the reference arm, hence allowing detection of the interference between the light reflected from the glass coverslip (standard coverslips, 170 μm thick, $n = 1.52$, P24-1.5H-N, Cellvis, Canada) and the light backscattered by the different depths of the sample. The top surface of the glass coverslip here acts as the reference mirror and is slightly defocused compared to the focal plane of the objective. The reflectivity of the glass in water is about 0.4%, according to Fresnel coefficients and neglecting angular effects.

For both configurations, the Q-2HFW camera was configured to have a FWC of 1.6 Me^- . Acquisitions were performed at 100 frames per second (FPS) when generating dynamic images. All samples were imaged inside a top-stage microincubator (H201-K-FRAME, H201-MW-HOLDER and OBJ-COLLAR-2532, Okolab, Italy) and were maintained at 37 $^\circ\text{C}$ and 5% of CO_2 concentration during the acquisition. Data were acquired with a custom Matlab graphical user interface enabling continuous data logging while post-processing and saving the resulting metrics in parallel threads for maximal acquisition speed [16].

2.2. Image acquisition protocol and dynamic FFOCT image generation

The dynamic images showcased were computed according to three metrics established by Scholler *et al.* in 2020 [23] using either 512 raw FFOCT or iSR FFOCT images and computing the mean frequency of the power density spectrum (Hue channel controlling the color), the standard deviation frequency of the power density spectrum (Saturation channel) and the averaged running standard deviation with a window of 50 images (Brightness channel), displayed together in a Hue Saturation and Brightness (HSB) base, respectively. The data workflow was established by Monfort *et al.* 2023 [16], resulting in effectively one dynamic HSB set every 5.12 s when time lapsing on the same field of view, or 7 s when mosaicking and/or ZStacking.

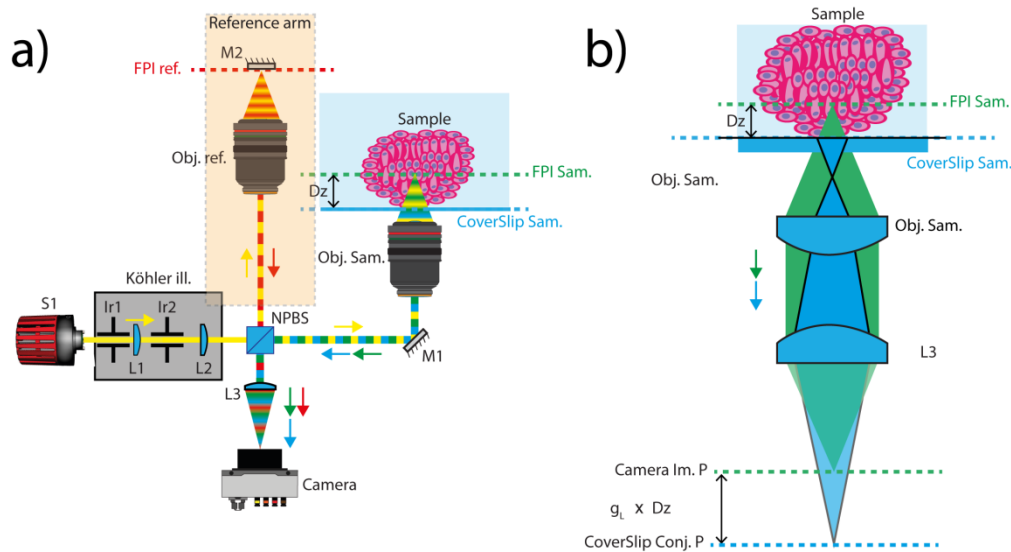


Fig. 1. Comparison between D-FFOCT setup versus iSR D-FFOCT. Fig. 1a illustrates a classic D-FFOCT setup with a spatially incoherent source (mounted LED, Thorlabs, $\lambda_0 = 810$ nm, $\Delta\lambda = 25$ nm) illuminating a Linnik interferometer using a Köhler illumination. The incoming field, in yellow, is split by a non-polarizing beam splitter (NPBS, BS014, Thorlabs, Newport, NJ, USA) cube into a *reference arm* and a *sample arm*. In the reference arm, an objective focuses the light on a mirror, placed at the image focal plane (FPI ref.) of the reference objective (Obj. ref.). The back reflected field is sketched in red. In the sample arm, an identical microscope objective (Obj. Sam) focuses the light onto a sample, laid on a coverslip (CoverSlip Sam) for the inverted microscope, at its image focal plane (FPI Sam). The backscattered light is illustrated in green. The objective (Obj. Sam) also collects the out-of-focus light (pictured in blue) reflected by the specular top surface of the coverslip (CoverSlip Sam). The two beams are recombined by the NPBS and focused on a camera by intermediary of a tube lens L3. In iSR FFOCT, the reference arm is blocked so that only the two beams from the sample arm reach the camera and can interfere. The microscope objectives are 30X, 1.05 NA silicon oil Olympus objectives, and the tube lens an achromatic doublet of focal length 300 mm. Fig. 1b illustrates the iSR D-FFOCT configuration showing the imperfect overlap of these two beams occurring on the camera. Camera Im. P means camera image plane and CoverSlip Conj. P stands for the plane conjugated to the coverslip surface.

2.3. Volumetric acquisition protocol

In order to obtain 3D stacks of static and dynamic contrast, the strategies differ slightly between FFOCT and iSR FFOCT. A first image is acquired at an initial axial position. For a static FFOCT acquisition, a 4-phase stepping algorithm is used. For dynamic FFOCT and iSR FFOCT, 512 images are acquired for each plane without modulation of the reference arm, and the signal fluctuations are analyzed as described above. Then, the sample holder is translated axially to reach a second position. The refractive index of the sample can be considered to correct for the index mismatch and the associated defocus aberration [39]. In (D) FFOCT, this axial translation corresponds to reducing the propagation in the silicon oil ($n = 1.4$), and a longer propagation in the sample ($n \sim 1.36$), so that the reference arm length has to be reduced to match the coherence volume to this new position. In iSR (D) FFOCT, all the measurements are performed within the same coherence volume, so that no adjustment is required. A new image is acquired at this second position, and so on and so forth. Finally, in order to achieve static iSR FFOCT, 4 intensity

images are acquired at 4 successive positions taken at axial steps corresponding to a $\frac{\pi}{2}$ phase shift.

2.4. Fibroblast culture protocol

Human dermal fibroblasts from a healthy subject (male, 49 y.o, Caucasian) were obtained at the Quinze-Vingts hospital after a skin biopsy. Fibroblasts were cultured in T75 flasks in DMEM glutamax medium (Thermo Fisher Scientific, 61965026) supplemented with 10% Fetal Bovine Serum (FBS), 2% sodium pyruvate, 1% penicillin-streptomycin and 1% amphotericin B, and incubated at 37°C, in a 5% CO₂ incubator. When fibroblasts reached 70% confluency, cells were dissociated using Enzyme Express (1X) TrypLE (Thermo Fisher Scientific, 12605010). Cells were plated in an uncoated 6-well glass bottom plate (Cellvis, P06-1.5H_N) at a density of 40 000 cells/well and the medium was changed every 2 days. Five days after seeding, fibroblasts were imaged.

3. Results and discussion

3.1. System characterization: resolution, and sensitivity

With iSR FFOCT, we successfully obtained static images of fibroblasts by recording and subtracting two successive planes so that a phase difference of $\frac{\pi}{2}$ is obtained (not shown). We also obtained dynamic images of fibroblasts (Fig. 2–5). Interestingly, in iSR D-FFOCT fibroblasts show many small, distinguishable, highly contrasted features, such as filopodia. Filopodia are cylindrical dynamic structures of around 100 to 300 nm diameter [40], below the diffraction limit, that can be used to characterize the optical system. Because filopodia are attached to the coverslip, they cannot be seen in D-FFOCT due to the fringe artefacts. For all characterizations in subsections 3.1 and 3.2, we only use and display the Brightness channel of the D-FFOCT or iSR D-FFOCT images.

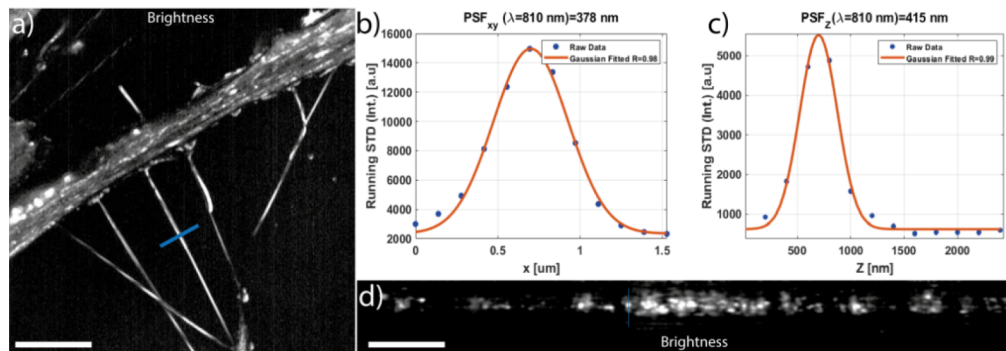


Fig. 2. Evaluation of iSR D-FFOCT spatial resolution using filipodia, which are sub-diffraction limit sized structures. Fig.2a shows an image including filipodia from which an intensity profile is displayed and fitted to a Gaussian in Fig.2b, with a half-width at the half-maximum (HWHM) of 378.4 nm. Fig.2d. shows an axial reslicing of a z stack including filipodia from which an intensity profile is displayed and fitted to a Gaussian in Fig.2c, with a full-width at the half-maximum (FWHM) of 415 nm. Intensity profiles displayed in Fig. 2(b)-(c) are highlighted by a blue line in Fig. 2(a) and, respectively. Scale bar in Fig. 2(a) is 44 μ m and 10 μ m in Fig. 2(d).

Evaluation of the optical response of the system along the transverse and axial dimensions was performed on such filipodia (Fig. 2). We obtained a very good Gaussian fit ($R > 0.98$) for both PSFs at 600 nm depth, and measured $PSF_{x,y}(\lambda = 810 \text{ nm}) = 378.4 \text{ nm}$ and $PSF_z(\lambda =$

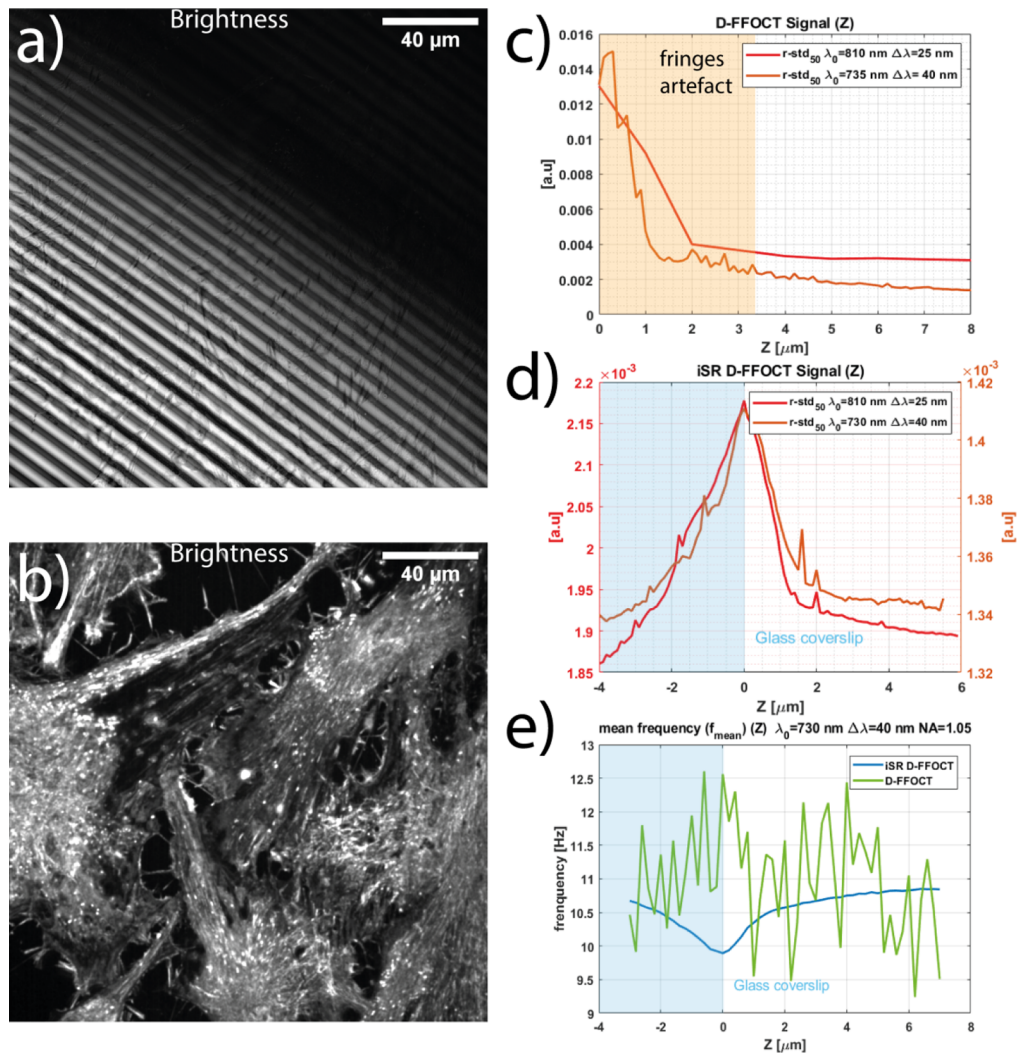


Fig. 3. Illustration of differences between D-FFOCT and iSR D-FFOCT. Two en-face images at the same location and depth ($\Delta Z = 0.8 \mu\text{m}$) are displayed using D-FFOCT (a) and iSR D-FFOCT (b). No fringe artefacts are present when using iSR D-FFOCT (b) unlike D-FFOCT (a). Signal strength (Brightness) is evaluated at different distances from the coverslip (ΔZ), on a 3D sample using D-FFOCT (c) and iSR D-FFOCT (d) with an 810 nm source (blue traces) and a 730 nm source (orange traces). e: Stability of D-FFOCT (orange trace) and iSR D-FFOCT (blue trace) is assessed using the mean frequency (Hue) at different depths using the LED at 730 nm.

810 nm) = 415 nm close to the theoretical values for the transverse resolution established for FFOCT [41], at high NA (NA > 0.6), limited by diffraction [41]:

$$PSF_{theo., x,y} = 0.512 * \frac{\lambda}{NA} = 395 \text{ nm at HWHM}$$

$$PSF_{theo., z} (NA > 0.6,) = \frac{0.44\lambda}{n(1 - \cos(\text{asin}(NA/n)))} = 752 \text{ nm at FWHM}$$

We found that iSR D-FFOCT has a narrower axial optical response than the expected theoretical response for static FFOCT, which we cannot explain at this stage. However, we note that no theoretical model has been established for D-FFOCT in general and no PSF evaluation was previously measured in the literature, to the best of our knowledge. We expect that the transverse and axial resolution of iSR D-FFOCT and of D-FFOCT are identical, but cannot find any dynamic sub-diffraction limit object easily observed in D-FFOCT (in contrast to the filopodia measured here) to validate such hypothesis. We can propose two possible explanations for D-FFOCT enhanced resolution. First, it was recently shown that due to the spatial incoherence properties of the light used in FFOCT, FFOCT optical response in absence of aberrations and at smaller NA, scales as the point spread function squared, as in ideal confocal microscopy [42]. The effect of spatial incoherence of the axial response, especially at high NA, when the optical sectioning is controlled by the aperture, still remains to be investigated theoretically. Second, because D-FFOCT contrast relies on the non-linear post-processing of multiple images, and especially on the calculation of the standard deviation of independently fluctuating scatterers, we may expect that D-FFOCT axial resolution can be increased in a similar way as in superresolution optical fluctuation imaging (SOFI) [43]. The theoretical investigation of how SOFI should be modified in an interferometric setting, and explaining why it may only enhance the axial resolution should be investigated. A more thorough theoretical and experimental understanding of the optical response in D-FFOCT and iSR D-FFOCT, and how it may depend on the SNR, and on the stochastic diffusion of the scatterer will be the object of future work.

Otherwise, iSR FFOCT can be described as a standard FFOCT system, with a defocused reference arm. Interestingly, it was recently shown that FFOCT resolution was almost insensitive to defocus [4,44], so that the effect of the defocus mostly results in a loss of signal rather than affecting the transverse resolution. As in FFOCT at such high resolution, the axial resolution is determined by an aperture effect, and does not depend on the spectral bandwidth. Still, a coherent laser source would not be ideal for imaging in (iSR) FF-OCT, because the spatial incoherence is important for cross talk rejection and resolution, and monochromatic sources can also show parasitic interference with other surfaces, such as the coverslip top surface, or optical elements surfaces.

In fibroblasts, we obtained a maximal sensitivity of 43.52 dB. Compared to standard D-FFOCT, the reference mirror in iSR D-FFOCT is made of glass of about 0.4% reflectivity, which can increase D-FFOCT sensitivity as long as incoherent reflections are lower than this value (See Annex), and provided the camera FWC can be saturated. Here, we used a NPBS to combine iSR D-FFOCT and a standard D-FFOCT system. However, incoherent reflections coming from the NPBS cube were very important when using a specular glass/sample reflection to create a reference field, and still filled up the FWC of our camera: about 92% of the dynamic range of our camera comes from incoherent reflections, of which 99% originates from the NPBS. These values were established by iteratively blocking out contributions from optics and/or the sample. We further note that the FFOCT configuration used in this paper picks up less incoherent reflection from the NPBS than the standard setup [16]. Because iSR D-FFOCT is immune to mechanical vibrations, a pellicle beamsplitter could be better suited to increase the theoretical sensitivity by a factor of 12. However, more powerful light source would be required and its integration in an

FFOCT microscope would be more complex. A mathematical comparison between FFOCT and iSR FFOCT as well as a discussion of the accessible contrast is proposed in the annex.

3.2. System advantages compared to D-FFOCT: fringe artefacts, vibration sensitivity and mosaicking

We first start by co-characterising iSR D-FFOCT and D-FFOCT responses in the vicinity of the coverslip, on the same areas and at the same distances from the coverslip/sample interface (ΔZ). Fig. 3(a)-(b) show images at the same locations at $\Delta Z = 0.8 \mu\text{m}$, illustrating that iSR D-FFOCT contrast (Fig. 3(b)), in the vicinity of a coverslip, is free of fringe-artefacts in comparison to D-FFOCT (Fig. 3(a), and [Visualization 1](#) and [Visualization 2](#)) while displaying significant structural details, including nuclei, nucleoli, mitochondria, filipodia and the actin filament network (see subsection 3.3). We recorded additional Z-stacks with axial steps of 100 nm for a larger axial range of about 10 μm using both iSR D-FFOCT and D-FFOCT in order to characterise their axial signal response. We found that iSR D-FFOCT (Fig. 3(d)) maintains sufficient contrast up to $\Delta Z = 3.5 \mu\text{m}$ while D-FFOCT only becomes fringe-free from this distance (Fig. 3(c)).

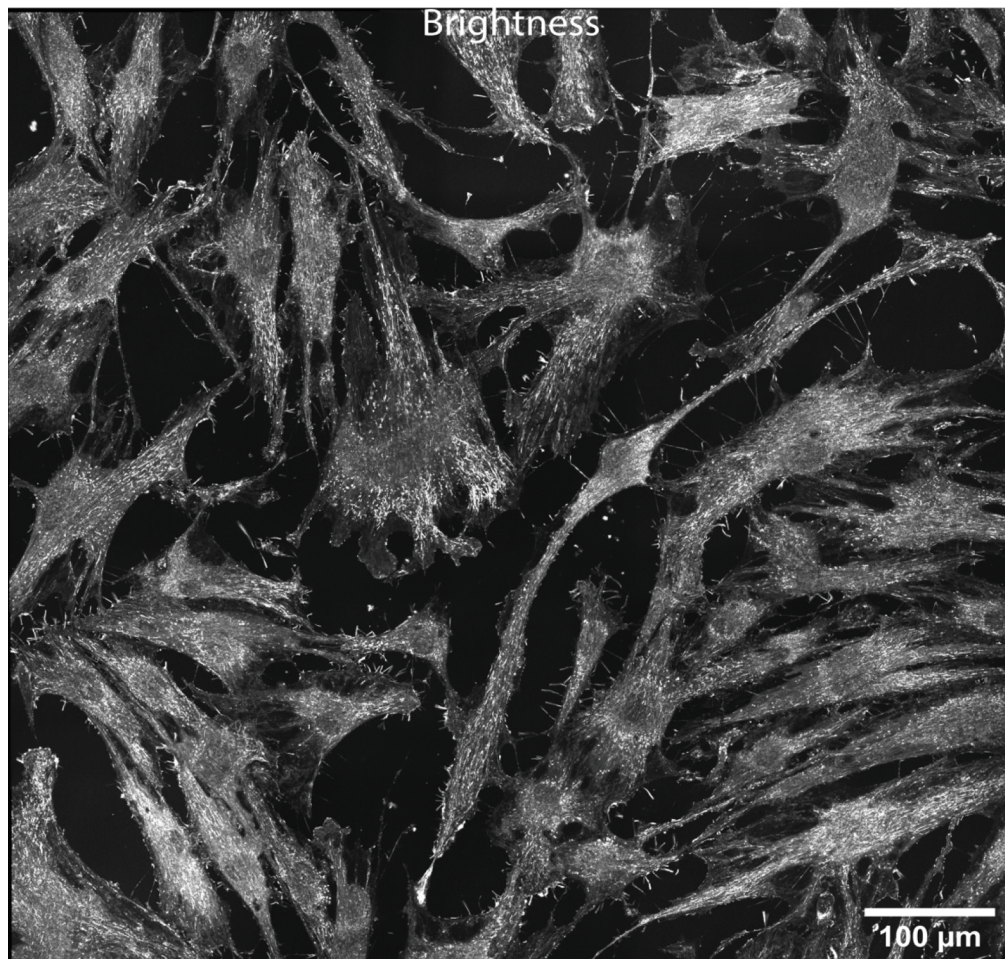


Fig. 4. iSR D-FFOCT (Brightness) mosaic of fibroblasts composed of 5×5 tiles with 20% overlap without numerical filtering. No overlap artefact nor image field distortions were observed confirming uniformness and flatness of iSR D-FFOCT signal.

In the case of D-FFOCT (Fig. 3(c)), we observe a strong signal (Brightness) in the vicinity of the glass coverslip due to the glass/culture medium interface reflection being significantly higher than light scattered by the sample, before dropping to a level where the glass coverslip and sample contribution are equivalent. These two behaviours are highlighted in Fig. 3(c) by an orange shaded area, corresponding to the depths where D-FFOCT is not able to image samples. In the case of iSR D-FFOCT, the signal is maximal at the glass coverslip interface and drops with depth (Visualization 1 and Visualization 2).

Furthermore, we assess the relative immunity of iSR D-FFOCT to mechanical vibration compared to D-FFOCT (Fig. 3(e)), by measuring how the averaged mean frequency of the power spectrum density (Hue channel) evolves during a Z-stack, at the equivalent depths and location. An improvement factor of 42.08 dB is found for iSR D-FFOCT over D-FFOCT in term of mean frequency stability (Hue). Indeed, the close distance ΔZ between the scatterer and the specular reflection, used to generate a reference field, seems to mechanically correlate the two. As a result, phase shifts due to vibrations stack up identically in both the reference and scattered field. This mechanical locking results in a virtually vibration-insensitive D-FFOCT imaging modality: we did not observe artefacts even when intentionally knocking on the optical table. As a result, iSR D-FFOCT is automatically quantitative and can function without the use of a mechanically damped optical table.

Finally, iSR D-FFOCT is able to produce very homogeneous and flat interference compared to D-FFOCT [16], thanks to its insensitivity to setup-induced aberrations, and its low penetration depth. This aspect can clearly be seen when mosaicking, as shown in Fig. 4 and Fig. 5a, which shows a flawless mosaic over a wide field whilst using a basic stitching method [45]. Compared to previous work using 50% overlap between D-FFOCT tiles for mosaic reconstruction at the same magnification [16], using a high-end stitching method, we could use a lower overlap of 20%, and we foresee lower tile overlap to also be possible. Furthermore, because field aberrations are particularly problematic at high NA, and are difficult to correct, this suggests that iSR D-FFOCT could potentially be performed at higher NA than standard D-FFOCT [16], and it allows an easier addition of optical elements in the sample arm, such as dichroic filters to be combined with fluorescence or adaptive optics elements to compensate for aberrations.

3.3. *Biological results on fibroblasts*

We imaged fibroblasts, which are flat epithelial cells, with iSR D-FFOCT to highlight cell structures and to characterise iSR D-FFOCT imaging responses (Visualization 1). Morphologically, each fibroblast displays a nucleus, indicated by red arrows in Fig. 5a, b, d, f, with an average frequency of 5 Hz and a slight desaturation, indicating a less chaotic oscillation of the nucleus compared to its surroundings. The boundary of the nucleus could be observed at specific depths displaying a further desaturated contrast, highlighted by a dash line in Fig. 5d, f. Euchromatin structures, less heavily packed and more disorganized part of the chromatin, delineated by a drop in Saturation, were also observed (Fig. 5d, f). Furthermore, we observe a drop in Brightness in the cytoplasm, probably highlighting static organelles, indicated by pink arrows in Fig. 5c-d.

Bright dots, especially present in Fig. 5b-c, f, can be actively transported vesicles or stressed mitochondria as previously identified using immunochemistry labelling and cross correlated to D-FFOCT [29]. Stress fibers linked to sites of adhesion and composed of long actin-filament bundles crossing cell bodies can also be observed as blue filaments at 3 Hz (Fig. 5(b), 5c, grey arrows) [46]. Moreover, filipodia which are protrusions of cytoplasm from lamellipodia, observed during cell migration, were distinguished by their high saturation and high dynamic activity at 9-13 Hz (red bundles) and by their oriented bundle of dynamic actin filaments [30] (Fig. 5(a),(b),d,e, yellow arrows). Their contrast has also been specifically cross correlated with dynamic D-FFOCT and immunofluorescence [29].

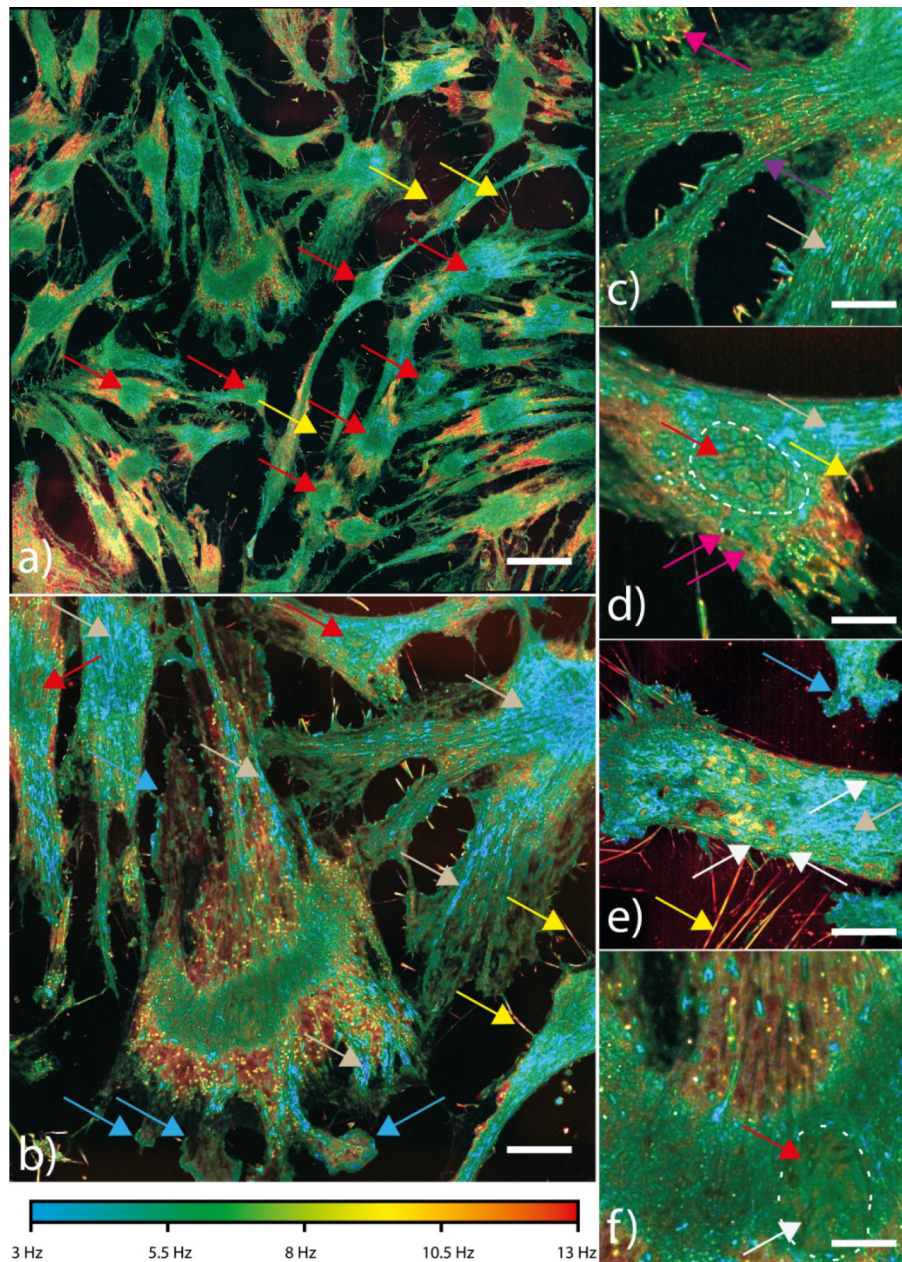


Fig. 5. Fibroblast structural analysis using iSR D-FFOCT. Fig.5a shows an iSR D-FFOCT HSB mosaic of fibroblasts composed of 5×5 tiles with 20% overlap. Hue scales from 3 to 13 Hz. Examples of nuclei observed are highlighted by red arrows in Fig.5a. Fig.5b highlights cases of lamellipodia structures (blue arrows). Fig.5c shows actin fibres, one example highlighted with a purple arrow. Euchromatin structures can be observed in Fig.5d within the nucleus, delimited by a white dashed line. Sharp membrane ridges and curved membrane pockets (white arrows) are shown in Fig.5e, as well as ridges in a nucleus in Fig.5f, delimited by a white dashed line. Examples of static organelles are highlighted by pink arrows in Fig.5c-d. Slowly varying stress fibers (blue filaments shown by grey arrows) are also visible. An example of a filipodium is highlighted in Fig.5e with a yellow arrow. Scale bar is $90 \mu\text{m}$ for Fig.5a, $40 \mu\text{m}$ for Fig.5b, $20 \mu\text{m}$ for Fig.5c, $15 \mu\text{m}$ for Fig.5d, $30 \mu\text{m}$ for Fig.5e and $15 \mu\text{m}$ for Fig.5f

Strikingly, Fig.5c-f display structures resembling the observations made in transmission electron microscopy (TEM), a super resolution invasive imaging technique, by Ghilardi et al. (2021) on fibroblasts [35]. In particular, membrane can be observed on the edge of the fibroblast, with a ridge-like appearance (indicated by a white arrow in Fig. 5(e)). Further comparison with this work, including comparison with specific fluorescence staining images, enables identification of actin fibres (Fig.5c, purple arrow). Lamellipodia, which guide cell movement, sensing the outer environment and extracellular stimuli, are clearly visualized in our images, with pronounced broad desaturation protrusions (Fig.5b, e, blue arrows).

Overall, these results show that iSR D-FFOCT is able to detect a wide variety of cytoplasm components, cell body shape and nuclear structures in cells, showing the potential of iSR D-FFOCT for label-free and non-invasive live assessment at high resolution. Furthermore, this demonstrates that iSR D-FFOCT can be used for thin 2D cell culture imaging.

4. Conclusion

In this work, we have developed a modified self-referenced configuration of *static* and *dynamic* FFOCT. This configuration is immune to fringe artefacts and mechanical vibrations. It is also less sensitive to interferometer arm misalignment and field curvature that can be critical with the use of very high NA objectives. It is simple to implement, especially on an existing D-FFOCT setup. Although the proposed design resembles to a classical widefield high NA microscope in reflection, using an interferometric scheme has 3 advantages. First, of minor importance, it slightly boosts the backscattered signal since the interfering term depends on $\sqrt{R_g R_c}$ with R_g about 10 times higher than the backscattered signal (see Annex), which facilitates the detection of small scatterers. Second, the theoretical axial resolution is about twice larger than the depth of field (depth of field of 1.47 μm simulated by a scalar based diffraction model versus 0.75 μm in Ref. [41] in interferometry). Finally, the most important feature is the phase sensitivity provided by the interferometry. It enables to access nanometric axial displacements of organelles inside cells, which is central to the dynamic signal we compute. We expect that such a contrast should not be observed in a standard widefield microscope.

Cytology plays an important role in diagnosing and managing human diseases. At a molecular level, the 'state' of a cell will depend on a large number of microscopic variables [47]. Moreover, most of the methods for measuring molecular state variables are destructive to cells, rendering it impossible to study temporal variation or correlate molecular states with downstream behaviour. In fact, organelle morphology can reflect neurological or metabolic diseases as well as cancers. For example, changes in mitochondrial morphology have been linked to several neurodegenerative disorders such as Alzheimer's [48], optic atrophy and Charcot-Marie-Tooth neuropathy [49]. Similar findings have been observed for the endoplasmic reticulum in pancreatic β -cells of type 2 diabetic patients [50]. At the nuclear level, changes in morphology have long been diagnostic of cancer with nuclear aberration correlated to the severity of prognosis [51]. A fast and easy analysis of subcellular structure with a non-invasive and live technique such as iSR D-FFOCT will contribute to enriching computational cytology and making a correct diagnosis. Moreover, this accessibility to image ultrastructure of live adherent cells will allow an efficient evaluation of new therapies targeting the pathological phenotype. Whilst similar analysis can be performed with other optical microscopies, in particular with quantitative phase imaging [8,9,52] and holotomography [53], these techniques are mostly restricted to thin and transparent samples. Although iSR D-FFOCT is restricted to shallow imaging depths within a few coherence lengths from the coverslip bottom surface, it does not require a transparent sample, and is mostly interesting for thin 2D samples, as well as for recording structures at the surface of a 3D sample (Visualization 2 in retinal organoid). These are situations where regular D-FFOCT typically struggles to obtain artefact-free images. We forecast that iSR D-FFOCT will be mainly interesting because it provides the same contrast as D-FFOCT in regions and samples where D-FFOCT

cannot achieve efficient imaging. It enables the validation of some observations made on explants or 3D cell models with D-FFOCT in 2D cell cultures models, which was not possible before.

Besides, by combining iSR D-FFOCT and D-FFOCT configurations, simply by blocking the reference arm at shallow depths, *static* and *dynamic* FFOCT images can now be continuously obtained over a depth range from the sample surface to a few hundred microns.

Thanks to its simplicity and its insensitivity to mechanical vibrations, iSR D-FFOCT could be deployed in much harsher environments than standard D-FFOCT, including operation rooms, classrooms, field measurements, or even within exploratory boats or zero-gravity environments, enabling the democratization of the use of D-FFOCT.

5. Annex: theoretical comparison between FF-OCT and iSR FF-OCT to account for the fringe artefacts and the sensitivity improvement

a. FF-OCT

In FF-OCT, as long as the glass coverslip stays within the coherence volume, the intensity received by the camera is the sum of the intensities from the reference arm, from the cell structures, and from the glass coverslip, and the sum of three interference terms:

$$I = I_0(R_r + R_g + R_c + 2\sqrt{R_r R_g} \cos\left(\frac{2\pi}{\lambda_0} \delta_{r-g}\right) \gamma(\delta_{r-g}) + 2\sqrt{R_r R_c} \cos\left(\frac{2\pi}{\lambda_0} \delta_{r-c}\right) \gamma(\delta_{r-c}) + 2\sqrt{R_g R_c} \cos\left(\frac{2\pi}{\lambda_0} \delta_{g-c}\right) \gamma(\delta_{g-c}))$$

Where, I_0 is the light intensity that would exit the interferometer if the reflectivity in both arms were 1. $R\{r,g,c\}$ are respectively the equivalent reflectivity of the reference mirror, of the interface between the glass coverslip and the culture medium (close to water in terms of optical properties) and of the cell structures. λ is the central wavelength of the source, γ is the coherence function of the detected light, and δ is the optical path difference between the different reflectors.

In a typical FF-OCT configuration, we have $R_r > R_g > R_c$, and in our case with a silicon wafer in the reference arm (because in thick samples, the reference reflectivity should be larger than the backscattering haze to optimize sensitivity), $R_r \sim 20\%$, $R_g \sim 0.44\%$, and $R_c \leq 10^{-4} - 10^{-6}$, hence:

$$R_r \sim 20\% \quad \sqrt{R_r R_g} \sim 3\% \quad \sqrt{R_r R_c} \sim 0.45\% \quad \sqrt{R_g R_c} \sim 0.06\%$$

The interference signal between the glass coverslip and the reference arm produces fringes with a contrast at least 10 times higher than the signal of interest coming from cells. In static FF-OCT, modulating the reference arm position also modulates the optical path difference with the glass coverslip, and the FF-OCT signal is dominated by the fringes. Due to this high contrast, even small phase variations (typically from mechanical noise) produce an intensity variation that gives a higher dynamic signal than cells, so that the fringe artefacts are also present in dynamic FF-OCT.

Besides, the sensitivity of FF-OCT is ultimately lowered due to the reflectivity of the glass coverslip. In FF-OCT, in a similar configuration with the coverslip outside the coherence volume, the minimum resolvable reflectivity R_{\min} can be written [41] as:

$$R_{\min} = \frac{(R_r + 2(R_{\text{inc}} + R_g))^2}{FWC \cdot N \cdot R_r}$$

Where R_{inc} is the equivalent reflectivity of all light coming from outside the coherence volume (i.e. reflections on optical elements, and scattering from other depths in the samples), FWC is the full well capacity of the camera and N , the number of frames summed. This formula is valid only when the light is close to saturating the camera. The maximum sensitivity is obtained when $R_r = 2(R_{\text{inc}} + R_g)$, as long as the camera can be saturated.

In a thin sample such as fibroblast cell cultures, the incoherent intensity is mostly limited to the reflections from the optical system, since the cell is mostly transparent. If such reflections are minimized, we can consider that $R_{inc} \sim 0$. Hence, the sensitivity is limited by the reflection from the glass coverslip, and the optimal value is:

$$R_{min} = \frac{16 R_g}{FWC \cdot N} \sim -74\text{dB per frame (i.e. for } N = 1)$$

b. *iSR FF-OCT*

In *iSR FF-OCT*, the reference arm is removed so that the interference term is composed only of the interference between the glass coverslip and the cell structure.

$$I_{ISR} = I_0(R_g + R_c + 2\sqrt{R_g R_c} \cos\left(\frac{2\pi}{\lambda_0} \delta_{g-c}\right) \gamma(\delta_{r-c}))$$

The remaining terms are the direct reflection by the glass coverslip $R_g \sim 0.44\%$ and the interference term between the light reflected by the coverslip and the light backscattered by the cell structure with $\sqrt{R_g R_c} \sim 0.06\%$. The interference term corresponding to the fringe artefacts has naturally disappeared, and the interference contrast remains high because the reflection on the coverslip has a similar intensity as the interference term. The price to pay is that only $\sim 0.1\%$ of the incident light (after the double pass in the beamsplitter) reaches the camera, so that a large number of photons needs to be sent to be able to saturate the camera. This may lead to increased photodamage, but in the case of cell imaging, it has to be mitigated by the small light-cell interaction in the near infrared. This may also lead to an increased influence of the incoherent reflections by the optical system (that may dominate), which would decrease the effective FWC, and lower the sensitivity. However, these optical reflections can be taken care of by appropriate optical designs.

In the ideal case, when the incoherent light is negligible, the minimum resolvable reflectivity R_{min} can become:

$$R_{min} = \frac{R_g}{FWC \cdot N} \sim 86 \text{ dB per frame}$$

Which corresponds to a sensitivity increase of a factor 16 compared to *FF-OCT* in similar conditions.

Funding. European Research Council (OPTORETINA(#101001841)); Agence Nationale de la Recherche (IHU FOReSIGHT [ANR-18-IAHU-0001], OREO [ANR-19-CE19-0023], VISCO [ANR-21-CE30-0024]).

Acknowledgement. We thank Jeremy Brogard and Marilou Cl  men  on for providing samples that allowed testing our microscope.

Author Contributions

The fibroblast imaging project was initiated by IA, KG and SR, and the optical challenges were identified by KG, OT and TM. The *iSR-DFFOCT* optical design was conceived by TM, supervised by OT, on a *D-FFOCT* setup developed by TM, OT, SA and KG. TM performed all optical engineering and proof of concept. Acquisition protocols were designed by TM and TBY, on samples provided by TBY, SR and IA. Acquisitions were performed by TM with assistance from SA. Images and volumes were reconstructed by TM on software designed and implemented by TM and OT. All authors discussed the results and wrote the article.

Disclosures. The authors declare that they have no known competing financial interests or personal relationships that could have appeared to influence the work reported in this paper.

Data availability. Data and codes are available upon reasonable request from the authors.

References

1. W. Drexler and J. Fujimoto, *Optical Coherence Tomography: Technology and Applications*, ser. Optical Coherence Tomography (Springer International Publishing, 2015).
2. O. Thouvenin, C. Boccarda, M. Fink, J. Sahel, M. P  ques, and K. Grieve, "Cell motility as contrast agent in retinal explant imaging with full-field optical coherence tomography," *Invest. Ophthalmol. Visual Sci.* **58**(11), 4605 (2017).
3. E. Dalimier and D. Salomon, "Full-field optical coherence tomography: a new technology for 3D high-resolution skin imaging," *Dermatology* **224**(1), 84–92 (2012).

4. A. Dubois, G. Moneron, K. Grieve, and A. C. Boccara, "Three-dimensional cellular-level imaging using full-field optical coherence tomography," *Phys. Med. Biol.* **49**(7), 1227–1234 (2004).
5. E. Beaurepaire, A. C. Boccara, M. Lebec, L. Blanchot, and H. Saint-Jalmes, "Full-field optical coherence microscopy," *Opt. Lett.* **23**(4), 244 (1998).
6. D. T. Miller and K. Kurokawa, "Cellular-scale imaging of transparent retinal structures and processes using adaptive optics optical coherence tomography," *Annu. Rev. Vis. Sci.* **6**(1), 115–148 (2020).
7. M. Choma, M. Sarunic, C. Yang, and J. Izatt, "Sensitivity advantage of swept source and Fourier domain optical coherence tomography," *Opt. Express* **11**(18), 2183 (2003).
8. M. A. Choma, A. K. Ellerbee, C. Yang, T. L. Creazzo, and J. A. Izatt, "Spectral-domain phase microscopy," *Opt. Lett.* **30**(10), 1162 (2005).
9. C. Joo, T. Akkin, B. Cense, B. H. Park, and J. F. de Boer, "Spectral-domain optical coherence phase microscopy for quantitative phase-contrast imaging," *Opt. Lett.* **30**(16), 2131 (2005).
10. D. Huang, E. A. Swanson, C. P. Lin, J. S. Schuman, W. G. Stinson, W. Chang, M. R. Hee, T. Flotte, K. Gregory, C. A. Puliafito, and J. G. Fujimoto, "Optical coherence tomography," *Science* **254**(5035), 1178–1181 (1991).
11. A. Fercher, C. Hitzenberger, G. Kamp, and S. El-Zaiat, "Measurement of intraocular distances by backscattering spectral interferometry," *Opt. Commun.* **117**(1-2), 43–48 (1995).
12. S. R. Chinn, E. A. Swanson, and J. G. Fujimoto, "Optical coherence tomography using a frequency-tunable optical source," *Opt. Lett.* **22**(5), 340 (1997).
13. J. F. de Boer, R. Leitgeb, and M. Wojtkowski, "Twenty-five years of optical coherence tomography: the paradigm shift in sensitivity and speed provided by fourier domain OCT [invited]," *Biomed. Opt. Express* **8**(7), 3248 (2017).
14. Y. Cai, K. Grieve, and P. Mécé, "Characterization and analysis of retinal axial motion at high spatiotemporal resolution and its implication for real-time correction in human retinal imaging," *Front. Med.* **9**, 868217 (2022).
15. O. Thouvenin, M. Fink, and A. C. Boccara, "Dynamic multimodal full-field optical coherence tomography and fluorescence structured illumination microscopy," *J. Biomed. Opt.* **22**(02), 1 (2017).
16. T. Monfort, S. Azzollini, J. Brogard, M. Cléménçon, A. Slembrouck-Brec, V. Forster, S. Picaud, O. Goureau, S. Reichman, O. Thouvenin, and K. Grieve, "Dynamic full-field optical coherence tomography module adapted to commercial microscopes for longitudinal in vitro cell culture study," 2023.
17. O. Thouvenin, K. Grieve, P. Xiao, C. Apelian, and A. C. Boccara, "En face coherence microscopy [invited]," *Biomed. Opt. Express* **8**(2), 622 (2017).
18. B. Karamata, P. Lambelet, M. Laubscher, R. P. Salathé, and T. Lasser, "Spatially incoherent illumination as a mechanism for cross-talk suppression in wide-field optical coherence tomography," *Opt. Lett.* **29**(7), 736 (2004).
19. J. B. Arous, "Single myelin fiber imaging in living rodents without labeling by deep optical coherence microscopy," *J. Biomed. Opt.* **16**(11), 119802 (2011).
20. P. Mécé, J. Scholler, K. Groux, and C. Boccara, "High-resolution in-vivo human retinal imaging using full-field OCT with optical stabilization of axial motion," *Biomed. Opt. Express* **11**(1), 492 (2020).
21. V. Mazlin, P. Xiao, E. Dalimier, K. Grieve, K. Irsch, J.-A. Sahel, M. Fink, and A. C. Boccara, "In vivo high resolution human corneal imaging using full-field optical coherence tomography," *Biomed. Opt. Express* **9**(2), 557 (2018).
22. J. Lee, W. Wu, J. Y. Jiang, B. Zhu, and D. A. Boas, "Dynamic light scattering optical coherence tomography," *Opt. Express* **20**(20), 22262 (2012).
23. J. Scholler, K. Groux, O. Goureau, J.-A. Sahel, M. Fink, S. Reichman, C. Boccara, and K. Grieve, "Dynamic full-field optical coherence tomography: 3d live-imaging of retinal organoids," *Light: Sci. Appl.* **9**(1), 140 (2020).
24. J. Scholler, V. Mazlin, O. Thouvenin, K. Groux, P. Xiao, J.-A. Sahel, M. Fink, C. Boccara, and K. Grieve, "Probing dynamic processes in the eye at multiple spatial and temporal scales with multimodal full field OCT," *Biomed. Opt. Express* **10**(2), 731 (2019).
25. C. Apelian, F. Harms, O. Thouvenin, and A. C. Boccara, "Dynamic full field optical coherence tomography: subcellular metabolic contrast revealed in tissues by interferometric signals temporal analysis," *Biomed. Opt. Express* **7**(4), 1511 (2016).
26. M. Jain, N. Shukla, M. Manzoor, S. Nadolny, and S. Mukherjee, "Modified full-field optical coherence tomography: A novel tool for rapid histology of tissues," *Journal of Pathology Informatics* **2**(1), 28 (2011).
27. M. Münter, M. vom Endt, M. Pieper, M. Casper, M. Ahrens, T. Kohlfaerber, R. Rahmanzadeh, P. König, G. Hüttmann, and H. Schulz-Hildebrandt, "Dynamic contrast in scanning microscopic OCT," *Opt. Lett.* **45**(17), 4766 (2020).
28. O. Thouvenin, J. Scholler, D. Mandache, M. C. Mathieu, A. B. Lakhdar, M. Darce, T. Monfort, C. Boccara, J.-C. Olivo-Marin, K. Grieve, V. M. Yedid, and E. B. a la Guillaume, "Automatic diagnosis and biopsy classification with dynamic full-field OCT and machine learning," May 2021.
29. K. Groux, A. Verschuere, C. Nanteau, M. Cléménçon, M. Fink, J.-A. Sahel, C. Boccara, M. Paques, S. Reichman, and K. Grieve, "Dynamic full-field optical coherence tomography allows live imaging of retinal pigment epithelium stress model," *Commun. Biol.* **5**(1), 575 (2022).
30. V. Mazlin, O. Thouvenin, S. Alhaddad, M. Boccara, and C. Boccara, "Label free optical transmission tomography for biosystems: intracellular structures and dynamics," *Biomed. Opt. Express* **13**(8), 4190 (2022).
31. O. Thouvenin, S. Alhaddad, V. Mazlin, M. Boccara, and C. Boccara, "Label free optical transmission tomography for biosystems: intracellular structures and dynamics," (2022).

32. M. Kapaczynska, T. Kolenda, W. Przybyta, M. Zajackowska, A. Teresiak, V. Filas, M. Ibbs, R. Blizniak, L. Lúczewski, and K. Lamperska, "2d and 3d cell cultures a comparison of different types of cancer cell cultures," *AOMS* **14**(4), 910–919 (2016).
33. S. Sanyal and M. Kosovsky, "Materials and assay systems used for three-dimensional cell culture," in *Technology Platforms for 3D Cell Culture: A User's Guide* (Wiley, 2017), pp. 143–172.
34. K. M. Yamada and E. Cukierman, "Modeling tissue morphogenesis and cancer in 3d," *Cell* **130**(4), 601–610 (2007).
35. S. J. Ghilardi, M. S. Aronson, and A. E. Sgro, "Ventral stress fibers induce plasma membrane deformation in human fibroblasts," mar 2021.
36. S. Jeknic, T. Kudo, and M. W. Covert, "Techniques for studying decoding of single cell dynamics," *Front. Immunol.* **10**, 755 (2019).
37. S. Aknoun, M. Yonnet, Z. Djabari, F. Graslin, M. Taylor, T. Pourcher, B. Wattellier, and P. Pognonec, "Quantitative phase microscopy for non-invasive live cell population monitoring," *Sci. Rep.* **11**(1), 4409 (2021).
38. T. Stephan, A. Roesch, D. Riedel, and S. Jakobs, "Live-cell STED nanoscopy of mitochondrial cristae," *Scientific Reports* **9**1, 12419 (2019).
39. J. Binding, J. B. Arous, J.-F. Léger, S. Gigan, C. Boccara, and L. Bourdieu, "Brain refractive index measured in vivo with high-NA defocus-corrected full-field OCT and consequences for two-photon microscopy," *Opt. Express* **19**(6), 4833 (2011).
40. P. K. Mattila and P. Lappalainen, "Filopodia: molecular architecture and cellular functions," *Nat. Rev. Mol. Cell Biol.* **9**(6), 446–454 (2008).
41. A. Dubois, L. Vabre, A.-C. Boccara, and E. Beaurepaire, "High-resolution full-field optical coherence tomography with a linnik microscope," *Appl. Opt.* **41**(4), 805 (2002).
42. V. Barolle, J. Scholler, P. Mécé, J. M. Chassot, K. Groux, M Fink, and A. Aubry, "Manifestation of aberrations in full-field optical coherence tomography," *Opt. Express* **29**(14), 22044–22065 (2021).
43. T. Dertinger, R. Colyer, G. Iyer, S. Weiss, and J Enderlein, "Fast, background-free, 3D super-resolution optical fluctuation imaging (SOFI)," *Proc. Natl. Acad. Sci. U. S. A.* **106**(52), 22287–22292 (2009).
44. P. Xiao, M. Fink, and A. C. Boccara, "Full-field spatially incoherent illumination interferometry: a spatial resolution almost insensitive to aberrations," *Opt. Lett.* **41**(17), 3920 (2016).
45. S. Preibisch, S. Saalfeld, and P. Tomancak, "Globally optimal stitching of tiled 3d microscopic image acquisitions," *Bioinformatics* **25**(11), 1463–1465 (2009).
46. S. Maiti, Cytoskeleton Actin-capping and Severing Proteins (Elsevier, 2021), pp. 167–180.
47. A. Y. Chang and W. F. Marshall, "Organelles understanding noise and heterogeneity in cell biology at an intermediate scale," *J. Cell Sci.* **130**(5), 819–826 (2017).
48. W. Qian, S. Choi, G. A. Gibson, S. C. Watkins, C. J. Bakkenist, and B. V. Houten, "Mitochondrial hyperfusion induced by loss of the fission protein drp1 causes ATM-dependent g2/m arrest and aneuploidy through DNA replication stress," *J. Cell Sci.* **125**(23), 5745–5757 (2012).
49. N. Cummins, C. A. Bartlett, M. Archer, E. Bartlett, J. M. Hemmi, A. R. Harvey, S. A. Dunlop, and M. Fitzgerald, "Changes to mitochondrial ultrastructure in optic nerve vulnerable to secondary degeneration in vivo are limited by irradiation at 670 nm," *BMC Neurosci.* **14**(1), 98 (2013).
50. J. D. Wikstrom, T. Israeli, E. Bachar-Wikstrom, A. Swisa, Y. Ariav, M. Waiss, D. Kaganovich, Y. Dor, E. Cerasi, and G. Leibowitz, "AMPK regulates ER morphology and function in stressed pancreatic -cells via phosphorylation of DRP1," *Molecular Endocrinology* **27**(10), 1706–1723 (2013).
51. E. S. Cibas and D. B. Cytology, "Diagnostic principles and clinical correlates," (2019).
52. Y. Park, C. Depeursinge, and G. Popescu, "Quantitative phase imaging in biomedicine," *Nat. Photonics* **12**(10), 578–589 (2018).
53. Y. Cotte, F. Toy, P. Jourdain, N. Pavillon, D. Boss, P. Magistretti, P. Marquet, and C. Depeursinge, "Marker-free phase nanoscopy," *Nat. Photonics* **7**(2), 113–117 (2013).